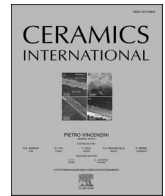




Contents lists available at ScienceDirect

Ceramics International

journal homepage: www.elsevier.com/locate/ceramint

Intrinsic and photocatalytic disinfection properties of CaTiO₃, SrTiO₃, and BaTiO₃ alkaline earth metal titanate perovskites

Tamás Gyulavári^{a,*}, Mahsa Abedi^a, Sarolta Tóth^b, Áron Ágoston^{a,c}, Gábor Veréb^d, Attila Bodor^b, Ákos Kukovecz^a, Zoltán Kónya^a, Katalin Perei^b, Zsolt Pap^{a,e,f,**}

^a Department of Applied and Environmental Chemistry, University of Szeged, Rerrich Béla Sqr. 1, 6720, Szeged, Hungary

^b Department of Biotechnology and Microbiology, University of Szeged, 6720, Szeged, Hungary

^c Department of Physical Chemistry and Materials Sciences, University of Szeged, H-6720, Aradi v.sqr.1, Szeged, Hungary

^d Institute of Biosystem Engineering, Faculty of Engineering, University of Szeged, Moszkvai Blvd. 9, 6720, Szeged, Hungary

^e Nanostructured Materials and Bio-Nano-Interfaces Center, Interdisciplinary Research Institute on Bio-Nano-Sciences, Babes-Bolyai University, T. Laurian 42, 400271, Cluj-Napoca, Romania

^f Centre for 3B, Babes-Bolyai University, Clinicilor 5-7, 400006, Cluj-Napoca, Romania

ARTICLE INFO

Handling Editor: Dr P. Vincenzini

Keywords:

Photocatalysis
Alkaline earth metal titanates
Phenol
Disinfection
E. coli
B. licheniformis

ABSTRACT

The use of alkaline earth metal titanate perovskites across various industries is increasing due to their wide application possibilities. However, this raises concerns regarding their potential environmental impact, including microorganisms living in or entering surface water bodies. Accordingly, calcium, strontium, and barium titanates were hydrothermally prepared to investigate their photocatalytic disinfection efficiency against Gram-negative *Escherichia coli* and Gram-positive *Bacillus licheniformis* bacteria under UV-A light irradiation. The photocatalysts were characterized by X-ray diffraction, scanning electron microscopy, diffuse reflectance spectroscopy, and infrared spectroscopy measurements. Their photocatalytic activity was also evaluated by the photocatalytic oxidation of phenol. Commercially available alkaline earth metal titanates were used as references. For phenol degradation, our strontium titanates had significantly better photoactivity than calcium and barium titanates ($\tau_0 = 41.60$ compared to 4.28 and $10.03 \times 10^{-10} \text{ M s}^{-1}$, respectively), while being considerably more efficient than the commercial references. This result was attributed to the presence of SrCO₃ acting as a co-catalyst, higher specific surface area, and more favorable band positions, enabling the generation of hydroxyl radicals. Disinfection results show that unmodified alkaline earth metal titanates have no or negligible disinfectant effect. Hydrothermally synthesized calcium and strontium titanates generated more hydroxyl radicals than the hydrothermally synthesized barium titanate and the references. For *E. coli*, the former samples had nearly identical disinfectant effect to UV-A light (~80 % bacterial inactivation over 2 h), while the other catalysts, which generated significantly fewer hydroxyl radicals, decreased the disinfection efficiency of UV-A light by ~40–70 % due to the catalyst particles screening the photons from bacteria. A similar trend was observed for *B. licheniformis* with higher disinfection efficiencies (100 % for UV-A light and the most efficient samples under 1 h) and higher activity reductions of ~30–100 %. These results contribute to the decision-making process regarding the risks associated with alkaline earth metal titanate perovskites in various industries.

1. Introduction

Titanate perovskites have received significant attention due to their promising properties making them suitable for ferroelectric, optoelectronics, piezoelectric, and photocatalytic applications [1,2]. For alkaline earth metal titanates, i.e., calcium titanate (CTO), strontium titanate

(STO), and barium titanate (BTO), these promising properties include low cost, nontoxicity, photocorrosion resistance, relatively high photoactivity (STO [3]), high dielectric constant (CTO [4]), and ferroelectricity, spontaneous polarization, and piezoelectricity (BTO [5]). The photocatalytic applicability of alkaline earth metal titanates has also been widely investigated for water splitting [6], water purification [4,

* Corresponding author.

** Corresponding author. Department of Applied and Environmental Chemistry, University of Szeged, Rerrich Béla Sqr. 1, 6720, Szeged, Hungary.

E-mail addresses: gyulavarit@chem.u-szeged.hu (T. Gyulavári), pszolt@chem.u-szeged.hu (Z. Pap).

<https://doi.org/10.1016/j.ceramint.2025.07.286>

Received 5 May 2025; Received in revised form 17 July 2025; Accepted 21 July 2025

Available online 21 July 2025

0272-8842/© 2025 The Authors. Published by Elsevier Ltd. This is an open access article under the CC BY-NC-ND license (<http://creativecommons.org/licenses/by-nc-nd/4.0/>).

7–12], air purification [13], hydrogen generation [14], metal reduction [11,15], CO₂ hydrogenation [16], and nitrogen fixation [14], just to name a few. For investigating photocatalytic water purification, most studies use dyes [17–19], and the potential photocatalytic disinfection efficiency of alkaline earth metal titanates is rarely studied [1].

It is well known that higher specific surface areas are desirable for photocatalytic applications [20], as photoinduced processes occur on the surface of catalysts [21]. Larger surfaces can be developed by decreasing the primary crystallite size, designing suitable morphologies [22] and layered structures [23,24]. However, nanosized particles pose greater environmental risks than macroscopic ones [25]. These risks include phytotoxicity, bioaccumulation in plants, acute and chronic diseases in humans and animals, and altered ecological niches of microbes [26,27]. It has also been shown that nanoparticles can undergo changes when released and exposed to soil, changing their mobility, bioavailability, and toxicity [28,29]. Toxicity for bacteria is manifested in their inactivation mediated by reactive oxygen species [30]. These species first initiate an external cell membrane attack [31,32], which presumably changes membrane permeability [33,34]. The compromised membrane gives rise to the leakage of small ions and molecules [35], followed by impaired respiration activity or damaged macromolecules (DNA, RNA, proteins) [36], finally leading to the lysis of the cell.

Based on the mechanism of the disinfection effect, related studies can be divided into different categories. Alkaline earth metal titanates can show a disinfection effect due to different mechanisms, which include, but are not limited to intrinsic [37], piezocatalytic [38,39], pyroelectric [40], photocatalytic [15,41], and phototermocatalytic [42] means. For CTO, the piezocatalytic disinfection efficiency of Ag/TiO₂/CTO composite [39] and photocatalytic antibacterial properties of Ag-modified CTO [15] have been investigated; however, in these works, CTO was either used as a composite constituent or modified with silver, which is well-known for its antibacterial effect. Similarly, for STO, the phototermocatalytic disinfection efficiency of Cu_xO/Ag/SrTiO₃ composite [42] and photocatalytic disinfection efficiency of Rh-doped STO under visible light have been widely investigated [8,43–45]. Last, for BTO, the piezocatalytic antibacterial effect with persulfate activation [38] or poled BTOs [46], pyroelectric radical formation with Pd-modified BTO [40], intrinsic disinfectant effect [37], and the photocatalytic disinfection effect of poled BaZrTiO₃ [41] have already been investigated. In all these works, the catalysts were either doped, modified with metal deposition, combined, or the disinfection was not carried out by photocatalytic means.

This study aims to systematically investigate the intrinsic and photocatalytic disinfection effect of hydrothermally synthesized CTO, STO, and BTO alkaline earth metal titanates using Gram-negative *E. coli* and Gram-positive *Bacillus licheniformis* bacteria. To the best of our knowledge, such a systematic investigation has not been carried out so far [1]. The photocatalytic oxidation activity using phenol as a model pollutant is also considered. Commercially available alkaline earth metal titanates are used as references. An attempt is also made to correlate characterization results with the photocatalytic activities observed.

2. Experimental

2.1. Materials

Strontium nitrate (Molar Chemicals, >99%), calcium nitrate (Sigma-Aldrich, 99%), and barium nitrate (Thermo Scientific, >99%) together with Aeroxide P25 TiO₂ (Acros Organics, >99.5%) were used as CTO, STO, and BTO precursors, respectively. Potassium hydroxide (VWR Chemicals, Ph. Eur.) was used to dissolve P25 TiO₂, and ultrapure water (Millipore Milli-Q) was used as the solvent. Phenol (Spektrum 3D, analytical grade), *E. coli* K12, and *Bacillus licheniformis* bacteria were used to evaluate photoactivity. Coumarin (Sigma Aldrich, >99%) was used to follow hydroxyl radical formation. Commercially available CTO (Sigma-Aldrich, 99%), STO (Alfa Aesar, 99%), and BTO (Sigma-

Aldrich, >99%) photocatalysts were used as references.

2.2. Synthesis

The alkaline earth metal titanates were synthesized following a hydrothermal method reported by Jiang et al. who prepared strontium titanates [47]. We tested several synthesis methods, but only with the abovementioned approach did we observe that by replacing the alkaline-earth-metal-containing starting material (which were nitrate salts in all cases for consistency and to minimize possible variables) we obtained a product with the desired crystallinity and purity. First, 18.75 mmol of alkaline earth metal nitrate was added to 30 mL of Milli-Q water under vigorous stirring. At the same time, in a separate beaker, 1.08 mol (60.59 g) of potassium hydroxide was slowly added to 60 mL of Milli-Q water. Second, 15 mmol (1.2 g) of P25 TiO₂ was dissolved in the potassium hydroxide solution after it cooled to room temperature. The reason for using excess alkaline earth metal salt (18.75 mmol) compared to P25 TiO₂ (15 mmol) was to prevent the formation of TiO₂ as a final product. Third, the contents of the two beakers were added together, and the mixture was stirred for 1 h. Then, the mixture was transferred into a 150 mL Teflon-lined stainless-steel autoclave and subjected to hydrothermal treatment for 12 h at 180 °C. Fourth, the product was washed two times with 96% ethanol and two times with Milli-Q water using centrifugation (4400 rpm, 15 min) to separate the nanoparticles after each washing cycle. Last, the catalyst was dried at 40 °C overnight and ground in an agate mortar.

Our samples were named “CTO-HT”, “STO-HT”, and “BTO-HT”, which refer to calcium, strontium, and barium titanate prepared via the hydrothermal method, respectively. The commercial references, in the same order, were named “CTO_Ref”, “STO_Ref”, and “BTO_Ref”.

2.3. Characterization methods and instrumentation

A Rigaku Miniflex II diffractometer was used to obtain X-ray diffraction (XRD) patterns for the investigation of crystalline composition by applying the following parameters: $\lambda_{\text{Cu K}\alpha} = 0.15406$ nm, 30 mA, 40 kV, 20–80 (2 θ) region. Average crystallite sizes were calculated using the Scherrer equation:

$$D = \frac{K \lambda_x}{\beta_{hkl} \cos \theta} \quad (1)$$

where D is the primary crystallite size, K is the shape factor (0.9), λ_x is the wavelength of the X-rays (0.15406 nm), β_{hkl} is the full width at half maximum, θ is the Bragg angle. A Hitachi S-4700 Type II microscope was used to take scanning electron microscopy (SEM) images for the investigation of morphology and calculation of aggregate size distribution histograms using an acceleration voltage of 10 kV. A Röntec QX2 detector was used applying a voltage of 20 kV to capture X-ray photons during SEM analysis for the investigation of chemical composition via energy-dispersive X-ray (EDX) analysis. A NOVA 3000e device was used to carry out 5-point nitrogen adsorption measurements for the investigation of specific surface areas using the Brunauer–Emmett–Teller (BET) method:

$$A_S = n_m a_m N_A \quad (2)$$

where A_S is the specific surface area, n_m is the monomolecular coverage, a_m is the cross-sectional area of the adsorbate (16.2×10^{-20} m² per adsorbed nitrogen molecule) and N_A is the Avogadro number (6.022×10^{23} mol⁻¹). A Shimadzu UV-3600 Plus spectrophotometer equipped with an integration sphere was used to carry out diffuse reflectance spectroscopy (DRS) measurements for the investigation of optical properties. The band gaps of the photocatalysts were obtained via the 1st-order derivative DR spectra [48]. A Bruker Vertex 70 FTIR instrument was used to record Fourier transform infrared (FTIR) spectra for the investigation of functional groups. The spectra were recorded

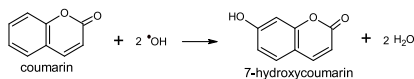
between the 400 and 4000 cm^{-1} range with a resolution of 4 cm^{-1} . A SPECS PHOIBOS 150 MCD system was used to carry out X-ray photoelectron spectroscopy (XPS) measurements and thus determine the valence band (E_{VB}) maximum values of the samples. The instrument consisted of a monochromatic Al-K α source (1486.6 eV), a hemispherical analyzer, and a charge neutralization device. The X-ray source was operated at 200 W, while the pressure of the analysis chamber ranged from 10^{-9} to 10^{-10} mbar. After determining the E_{VB} and band gap values, the conduction band (E_{CB}) minimum values were calculated following the $E_{\text{CB}} = E_{\text{VB}} + E_{\text{band gap}}$ equation.

2.4. Determination of photocatalytic activity

Phenol ($c_0 = 0.1$ mM) degradation experiments were carried out as follows. The photocatalyst ($m = 100$ mg) was added to the phenol solution ($V = 100$ mL), and after ultrasonication ($t = 5$ min) in an Ultrasonic PS 60A ultrasonication bath, the suspension was transferred into a double-walled glass photoreactor. The photoreactor was surrounded by six UV fluorescent tubes (Novelite T5, UV-A, 6 W; $\lambda_{\text{max}} = 365$ nm). The temperature was maintained at 25 °C, and a constant air supply was provided (to keep the dissolved oxygen level constant) during the 4-h-long measurements. Before turning on the lamps, the suspension was stirred in the dark for 15 min to reach adsorption–desorption equilibrium. Phenol concentration changes were followed by high-performance liquid chromatography (HPLC). The chromatograph consisted of a Merck Hitachi L-7100 low-pressure gradient pump and a Merck-Hitachi L-4250 UV–vis detector. A 50:50 (V/V) methanol/water mixture was used as the eluent, a LiChrospher C18 column was used as the stationary phase, and the absorbance values were recorded at $\lambda = 210$ nm.

Disinfection experiments with *Escherichia coli* and *Bacillus licheniformis* KK1 bacterial strains were conducted in the same photoreactor as the phenol degradation experiments. For this purpose, the photocatalyst was added to 100 mL of 0.9 wt% NaCl solution and homogenized by ultrasonication. This was followed by the addition of bacteria, which was prepared as follows. *E. coli* and *B. licheniformis* starter cultures were incubated in Luria-Bertani broth (LB: 10 g L $^{-1}$ tryptone, 10 g L $^{-1}$ NaCl, 5 g L $^{-1}$ yeast extract) on a rotary shaker (160 rpm) at 30 °C and 42 °C, respectively, until the OD $_{600}$ reached 1.0. The cells were centrifuged (13,000 rpm, 5 min, 4 °C), resuspended, and then diluted a hundredfold using a sterile 0.9 wt% NaCl solution. This cell suspension was added to the investigated solution (pH ~ 7) to reach the initial colony-forming unit (CFU) of approximately 10^4 CFU mL $^{-1}$. During the photocatalytic disinfection experiments, serial dilutions of each sample taken were plated onto LB agar media [49]. Last, CFUs were enumerated after a 2-day incubation at 25 °C to evaluate disinfection activity. Reproducibility data are expressed as mean \pm standard errors.

Hydroxyl radical generation was followed by the photocatalytic degradation of coumarin ($c_0 = 0.1$ mM), which yields 7-hydroxycoumarin (7-HC). The amount of fluorescent 7-HC formed corresponds to that of the hydroxyl radical generated. The measurements were conducted in the same photoreactor system as the phenol degradation and bacteria inactivation experiments. The amount of 7-HC formed was measured by photoluminescence (PL) measurements (Horiba Jobin Yvon Fluoromax-4), applying excitation and detection wavelengths of 350 and 453 nm, respectively.



3. Results and discussion

3.1. Structure, morphology, optical properties, and surface properties

First, the crystalline composition of our samples was investigated

and compared to that of the references. For the CTO samples (Fig. 1a), diffraction peaks at 23.32, 33.16, 47.56, 58.98, 59.36, 69.5, and 79.26 2θ can be attributed to the (101), (121), (202), (321), (123), (242), and (161) crystallographic planes of orthorhombic CTO (JCPDS No. 42–0423), respectively [4,50–52]. For the STO samples (Fig. 1b), reflections at 22.9, 32.4, 40.0, 46.4, 52.4, 57.7, 67.7, and 77.1 2θ correspond to the (100), (110), (111), (200), (210), (211), (220), and (311) crystallographic planes of cubic STO (JCPDS No. 35–0734), respectively [3,7,53]. For the BTO samples (Fig. 1c), diffraction peaks at 22.3°, 31.7°, 38.9°, 45.3°, 50.9°, 56.1°, and 65.8°, can be associated with the (100), (110), (111), (200), (210), (211), and (220) Miller indices of cubic BTO (JCPDS No. 31–0174) respectively [54,55]. In all our samples, the signals of carbonate impurities appeared: the one at 29.4° corresponds to CaCO_3 [56], the ones at 25.2° and 25.8° correspond to SrCO_3 [57,58], and the ones at 24.0° and 24.4° correspond to BaCO_3 [59,60]. Considering the peak areas of the most intense diffractions, these peaks amount to 4.9 %, 6 %, and 5.3 % carbonate contents in CTO_HT, STO_HT, and BTO_HT, respectively. Even the BTO_Ref sample contains a minor amount of BaCO_3 ; however, the signal-to-noise ratio is so low that it does not reach the limit of quantification. The appearance of these carbonate peaks can be explained by the presence of CO_2 in the air, which can react with potassium hydroxide resulting in the reaction of aqueous alkaline earth metal ions and carbonate ions [61,62]. Another possible source of carbonate impurities is the carbonate content (K_2CO_3) of the KOH used for the synthesis. It is known that carbonates can act as co-catalysts; however, their effect on photocatalytic activity is mixed. In our previous studies, we found that SrCO_3 in STO can increase the concentration of active species, enhancing the photocatalytic activity [3,63]; however, it can inhibit CH_4 and C_2H_6 production during the photoreduction of CO_2 [16,63]. Based on the Scherrer calculations and nitrogen adsorption measurements (Fig. S1), primary crystallite sizes were between 22.2 and 39.2 nm, while specific surface areas varied between 2.1 and 34.0 $\text{m}^2 \text{g}^{-1}$ (Table 1). In most cases, specific surface areas increased with decreasing primary crystallite sizes, as expected.

Second, the morphology of our samples and references were investigated, and the SEM micrographs with their corresponding size distribution histograms are shown in Fig. 2. The morphology of all reference alkaline earth metal titanates is similar: they contain shapeless, partly rounded, partly angular particles that cannot be characterized by a well-defined (secondary) morphology. The size distribution of the particles that make up the samples is also very similar: they are between 0.1 and 2 μm in all cases. In contrast, both the morphology and size distribution of our samples are very different. CTO_HT contains comparatively large aggregates of well-defined rectangular prisms, which is in agreement with the result for the specific surface area. The micrograph of STO_HT shows primary crystallites (in contrast with the aggregates of most of the other samples) with well-defined spherical morphology. The micrograph of BTO_HT shows both primary crystallites and aggregates. Please note that the size distribution histograms are only accurate for CTO_HT and STO_HT, while these values are only approximate for the rest of the samples due to their irregular morphologies.

Third, the optical properties of the samples were considered, and the DRS results are shown in Fig. 3. For the evaluation of band gaps, the first-order derivative method [48] was used. The most frequently reported band gap values for CTO, STO, and BTO are ~ 3.5 – 3.6 [52,64], ~ 3.2 [65,66], and ~ 3.2 [67,68] eV, respectively (although for BTO, these values range from 3.0 to 3.6 eV [1,69]). The band gaps obtained are in good agreement with these reported values. Based on them, all investigated samples are UV-active and cannot be excited by visible light.

Fourth, the surface properties of the samples were investigated by IR measurements, and the results are shown in Fig. 4. Overall, in the low wavenumber region (400–800 cm^{-1}), three bands can be observed in all samples: a smaller band at 430–450 cm^{-1} , a larger band at 550–610 cm^{-1} , and a shoulder centered at 640–710 cm^{-1} (which is not always well-defined). They can be attributed to the bending and stretching

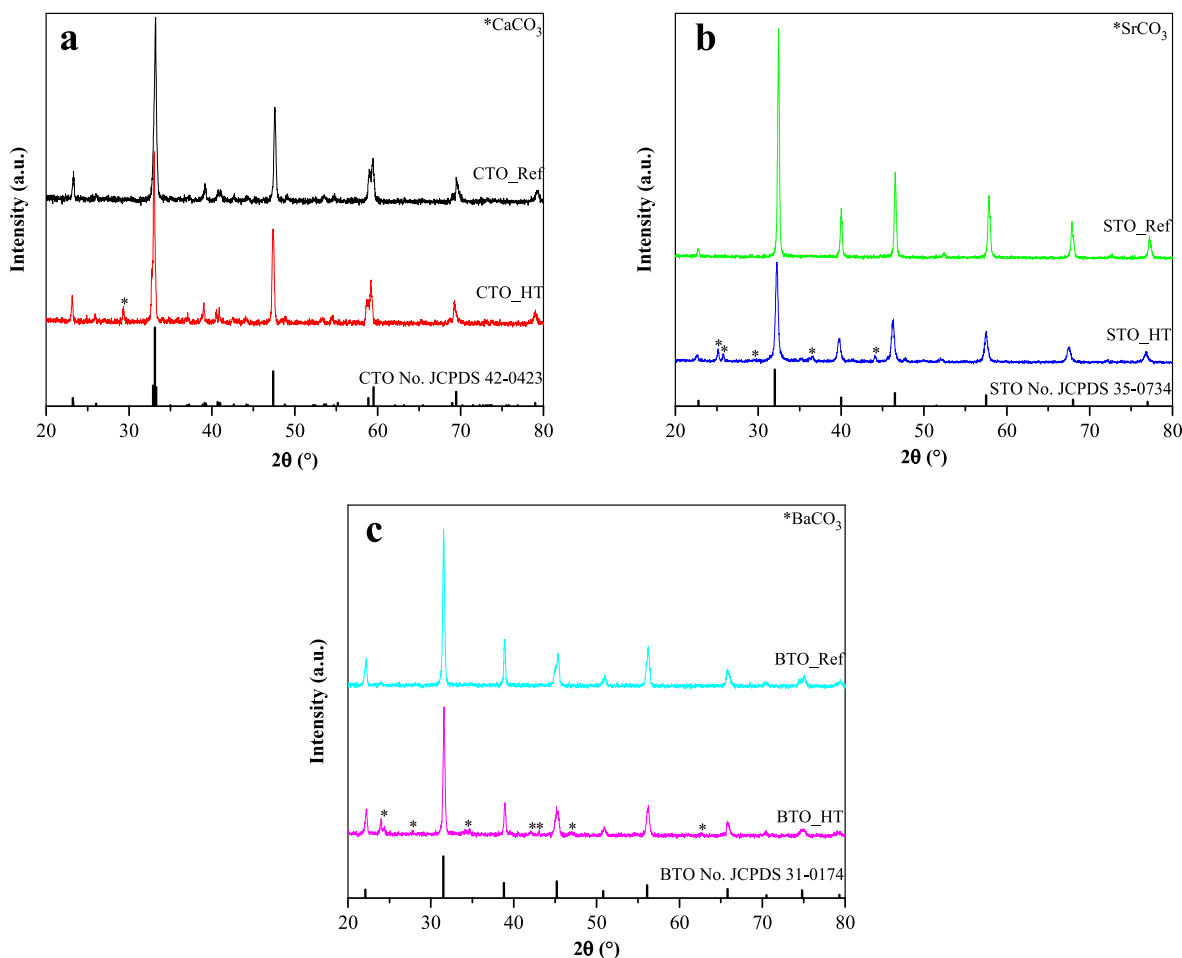


Fig. 1. XRD patterns of hydrothermally prepared and reference (a) calcium titanates, (b) strontium titanates, and (c) barium titanates.

Table 1

Size, band gap, specific surface area, and phenol degradation rates of the samples investigated.

Sample name	Mean crystallite size (nm)	Band gap (eV)	Specific surface area ($\text{m}^2 \text{g}^{-1}$)	$T_{0,\text{phenol}}$ (10^{-10}M s^{-1})
BTO_HT	33.4	3.26	24.1	10.03
BTO_Ref	31.8	3.25	11.5	8.89
STO_HT	22.2	3.35	34.0	41.60
STO_Ref	39.2	3.27	2.1	32.96
CTO_HT	36.8	3.51	2.4	4.28
CTO_Ref	31.7	3.63	3.3	9.99

vibrations of TiO_6 octahedra [70], Ti–O asymmetric stretching vibrations, and Ti–O–Ti asymmetric stretching vibrations, respectively [71]. Vibrations specific to the given alkaline earth metal titanate also appear in these regions: bands at 412, 576, and 745 cm^{-1} correspond to Ba–O [72], Ca– TiO_3 [73], and Sr–O [71] vibrations, respectively. The weak and narrow bands in our samples (i.e., in the non-reference samples) at $\sim 860\text{--}870 \text{ cm}^{-1}$ and the comparatively more intense and broader bands at $1430\text{--}1460 \text{ cm}^{-1}$ can be attributed to carbonates [74], which is consistent with the XRD results. These bands are present in BTO_Ref too with significantly lower intensities, which is also in good agreement with the XRD pattern observed because this is the only reference sample where a carbonate-specific reflection was observed. Last, the weak broad band centered at $\sim 3400 \text{ cm}^{-1}$ shows the stretching and bending vibrations of surface –OH/ H_2O groups [75,76].

Last, based on the DRS and XPS results, the E_{VB} , E_{CB} and band gap values were summarized in Table 2.

We found that our results for CTO are in good agreement with the literature, even though for STO_HT and BTO_HT, the differences are more significant. It is worth highlighting that these values are not consistent in the literature either. This statement is also supported by Fujisawa et al., who investigated the valence and conduction band edges of TiO_2 , SrTiO_3 , and BaTiO_3 [80]. Nevertheless, comparing the VB positions of our samples to the potential required for the $\text{H}_2\text{O}/\bullet\text{OH}$ reaction (i.e., 2.73 eV; [81,82]), it can be said that even though these potentials do not reach the potential required for hydroxyl radical generation, the order of the observed hydroxyl radical generation (i.e., $\text{STO_HT} > \text{CTO_HT} > \text{BTO_HT}$) is in good agreement with the order of these valence band positions. In other words, catalysts with valence band positions closer to the potential required for hydroxyl radical generation indeed generated more hydroxyl radicals.

3.2. Photocatalytic activity

3.2.1. Photocatalytic oxidation of phenol

The photocatalytic activity of the samples was evaluated not only via photocatalytic disinfection but via phenol degradation too (Fig. 5 and S2). In the absence of photocatalysts, only $\sim 3\%$ of phenol was degraded due to photolysis during the 4-h-long experiments. Since phenol is a weakly adsorbing molecule, no changes in its concentration were observed during the adsorption experiments (i.e., 15 min stirring in the dark). The CTO and BTO samples had low photoactivity: the conversion values observed were below 15% in all cases. In contrast, the STO samples performed significantly better. Our STO_HT sample degraded nearly twice as much phenol ($\sim 43\%$) than commercial STO_Ref (23%). The reason for these differences probably lies in the free radicals

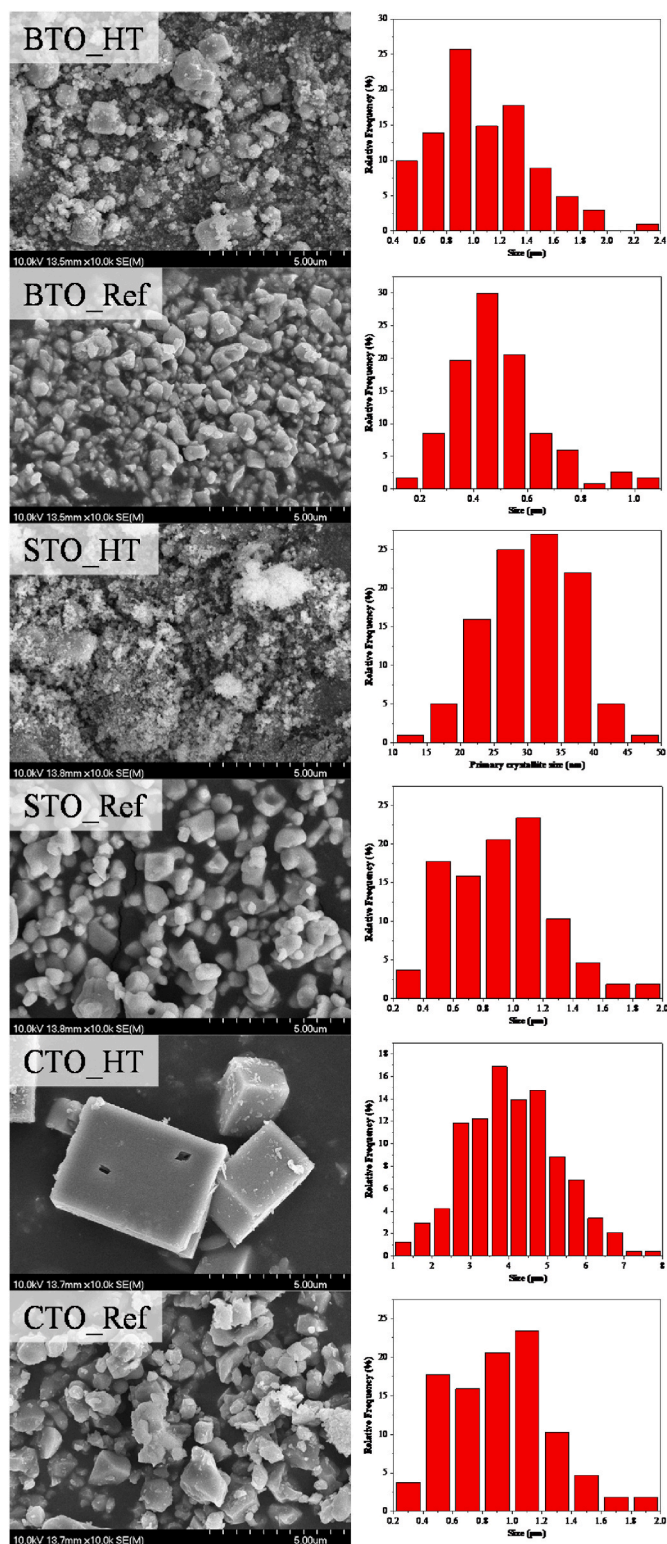


Fig. 2. SEM micrographs and corresponding size distribution histograms of hydrothermally prepared and reference alkaline earth metal titanates.

generated. It is known that reactive oxygen species are needed for the degradation of phenol. For example, reaction with hydroxyl radicals results in the formation of catechol and hydroquinone, while direct oxidation with holes results in the formation of resorcinol when TiO_2 is used [83]. Moreover, in our previous study, we found that catalysts with high disinfection efficiency have notable phenol degradation efficiency

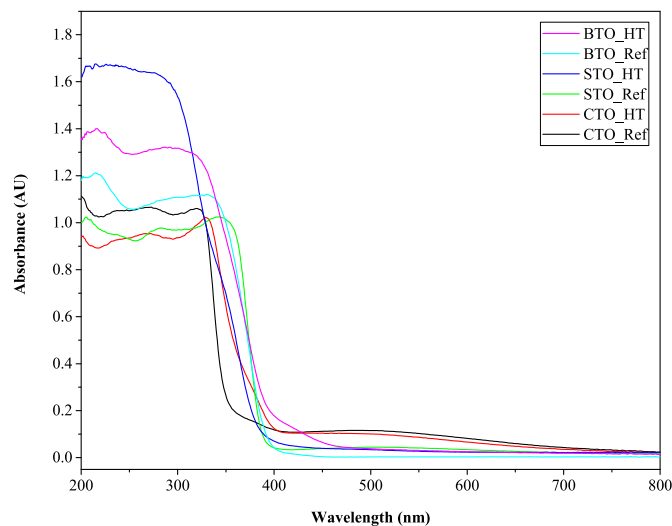


Fig. 3. Absorbance spectra of hydrothermally prepared and reference alkaline earth metal titanates.

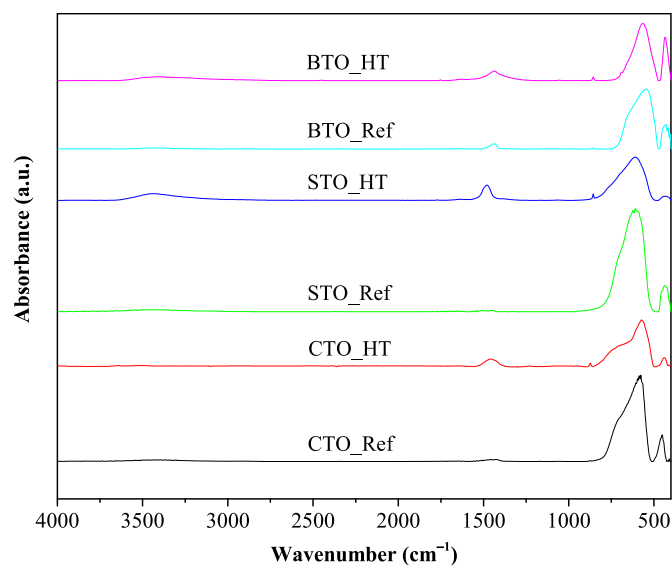


Fig. 4. IR spectra of hydrothermally prepared and reference alkaline earth metal titanates.

Table 2

Comparison of valence band, conduction band, and band gap values obtained in this study with literature data.

Sample name	E_{VB} (eV)	E_{CB} (eV)	Band gap (eV)	Reference
BTO_HT	1.51	-1.75	3.26	This study
BTO	2.28	-1.05	3.33	[77]
STO_HT	2.31	-1.04	3.35	This study
STO	2.91	-0.29	3.2	[78]
CTO_HT	2.17	-1.34	3.51	This study
CTO	2.05	-1.48	3.53	[79]

too; however, high phenol degradation efficiency does not necessarily translate to high disinfection efficiency [84]. It is also known that for the generation of hydroxyl radicals, the valence band maximum of photocatalysts must be more positive (i.e., in a lower position) than the potential required for the $\text{H}_2\text{O}/\bullet\text{OH}$ reaction (in the relative energy scale, i.e., vs E_{NHE}). Considering the band positions of alkaline earth metal titanates based on the literature (Fig. 5), the generation of hydroxyl

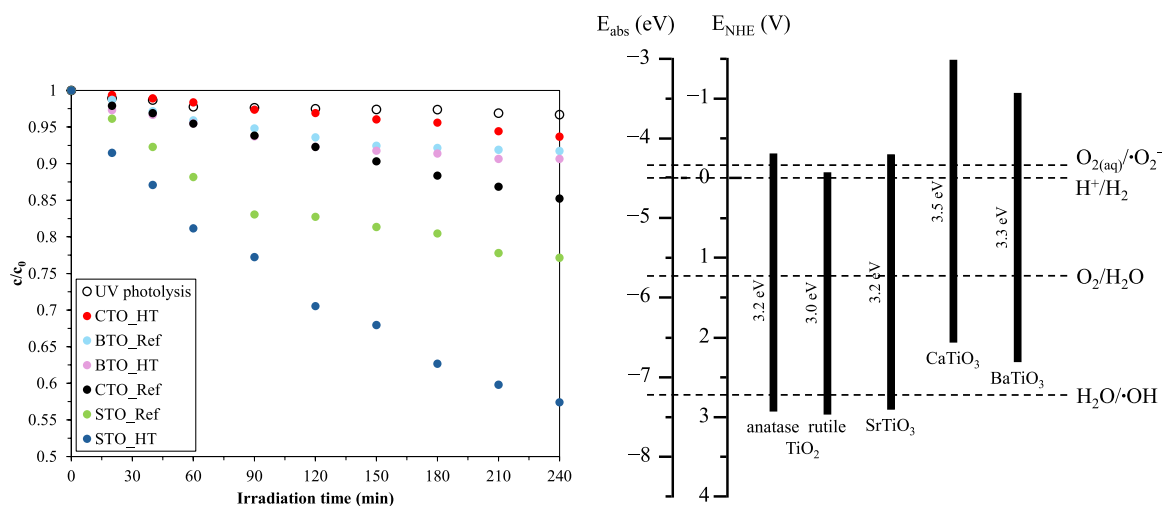


Fig. 5. Photocatalytic oxidation of phenol ($c_0 = 0.1$ mM) with alkaline earth metal titanates under UV-A light irradiation (left) and band positions [77–79,86] of alkaline earth metal titanates and titanium dioxide (right).

radicals is unfavored for CTO and BTO, whereas it is favored for STO. This statement was verified by detecting 7-HC formation via PL measurements during the degradation of coumarin (Fig. 6), as the reaction of coumarin with hydroxyl radicals produces fluorescent 7-HC [85]. The results show that initial hydroxyl radical generation is indeed the highest for the most efficient STO_HT sample. The decrease of 7-HC (corresponding to hydroxyl radical) amount generated over time can be explained by the catalysts also degrading the formed 7-HC. These results are in rather good agreement with the observed phenol degradation activity, partly explaining the overall low photoactivity of CTO and BTO and the comparatively higher photoactivity of STO.

3.2.2. Photocatalytic degradation mechanism

The mechanism of phenol degradation has been extensively investigated in the literature [87,88]. Based on the published results, the possible reactions and byproducts are summarized in Fig. 7.

During the phenol degradation experiments, hydroquinone formation was observed only for STO_HT (Fig. S6), which also supports the PL results. No significant differences were observed in the amounts and evolution trends. The formation of hydroquinone is possible due to the directing effect of the phenolic OH group on the benzene ring. This results in the attack of $\cdot OH$ radical at either the ortho or para positions, the

latter being the dominant one in this case. In summary, the HPLC and PL results prove the contribution of $\cdot OH$ radicals in the phenol degradation mechanism.

The higher photoactivity of STO_HT compared to STO_Ref can be attributed to several factors. One such factor is carbonate content. Based on our XRD and IR results, STO_HT contains SrCO₃, whereas STO_Ref does not. In our previous study, we investigated how carbonate impurities influence photoactivity [63]. In SrTiO₃-SrCO₃ composites, improved charge separation takes place: photogenerated electrons in the conduction band of SrTiO₃ move to the conduction band of SrCO₃ positioned at a slightly lower energy level. As a result, more holes remain in the valence band of STO (as the possibility of recombination is thus reduced), which can result in higher $\cdot OH$ concentrations. In this work, the results of radical scavenger experiments (investigating the role of h^+ , $\cdot O_2^-$, and $\cdot OH$ with ammonium oxalate, 1,4-benzoquinone, and isopropanol, respectively) showed that the involvement of $\cdot OH$ was the most pronounced. Moreover, based on in-situ EPR measurements, not only hydroxyl radicals but carbonate anion radicals can also form ($CO_3^{\cdot -}$), which are weaker oxidizing agents than $\cdot OH$ radicals, but can still contribute to photocatalytic degradation. Another factor influencing photoactivity is specific surface area. Based on our nitrogen adsorption and SEM results, we found that STO_HT has a significantly larger specific surface area than STO_Ref. The larger specific surface area of the former might contribute to the higher photoactivity by providing more active sites for photocatalytic reactions [20] (although this factor is less relevant due to the weak adsorption of phenol). Regarding the CTO and BTO samples, their very low photocatalytic activity prevents determining the mechanism reliably; thus, such investigation was not considered in this study.

3.2.3. Photocatalytic disinfection

The photocatalytic disinfection efficiency of the samples was investigated first by Gram-negative *E. coli* inactivation and the results obtained after 2 h of UV-A irradiation are shown in Fig. 8a. Similar to the phenol degradation results, our samples performed better than the reference samples in most cases. In the absence of catalysts, UV-A light alone already inactivated more than 80 % of *E. coli* bacteria over the course of the experiment. Somewhat surprisingly, the addition of most catalysts (except for STO_HT and CTO_HT) decreased the disinfection efficiency. This can be explained by the screening and scattering effect of catalyst particles ($c = 1$ g L⁻¹), blocking and absorbing the UV photons that activate them [89]. The fact that these catalysts (STO_Ref, CTO_Ref, BTO_Ref, and BTO_HT) generated only a comparatively low amount of

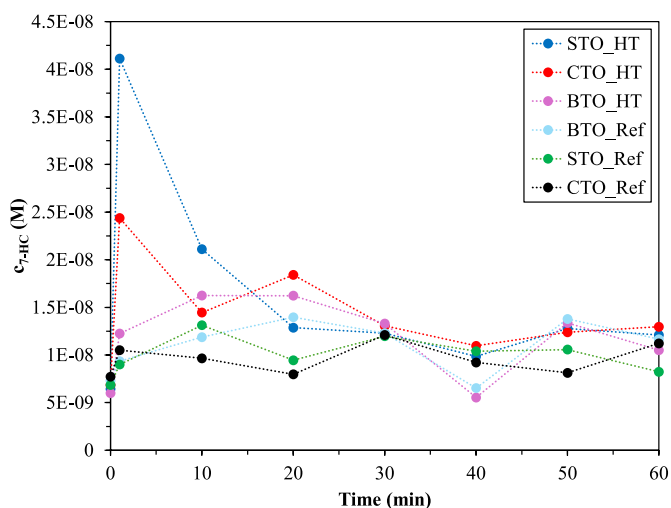


Fig. 6. Hydroxyl radical generation measured by fluorometric detection of 7-hydroxycoumarin formation during coumarin degradation.

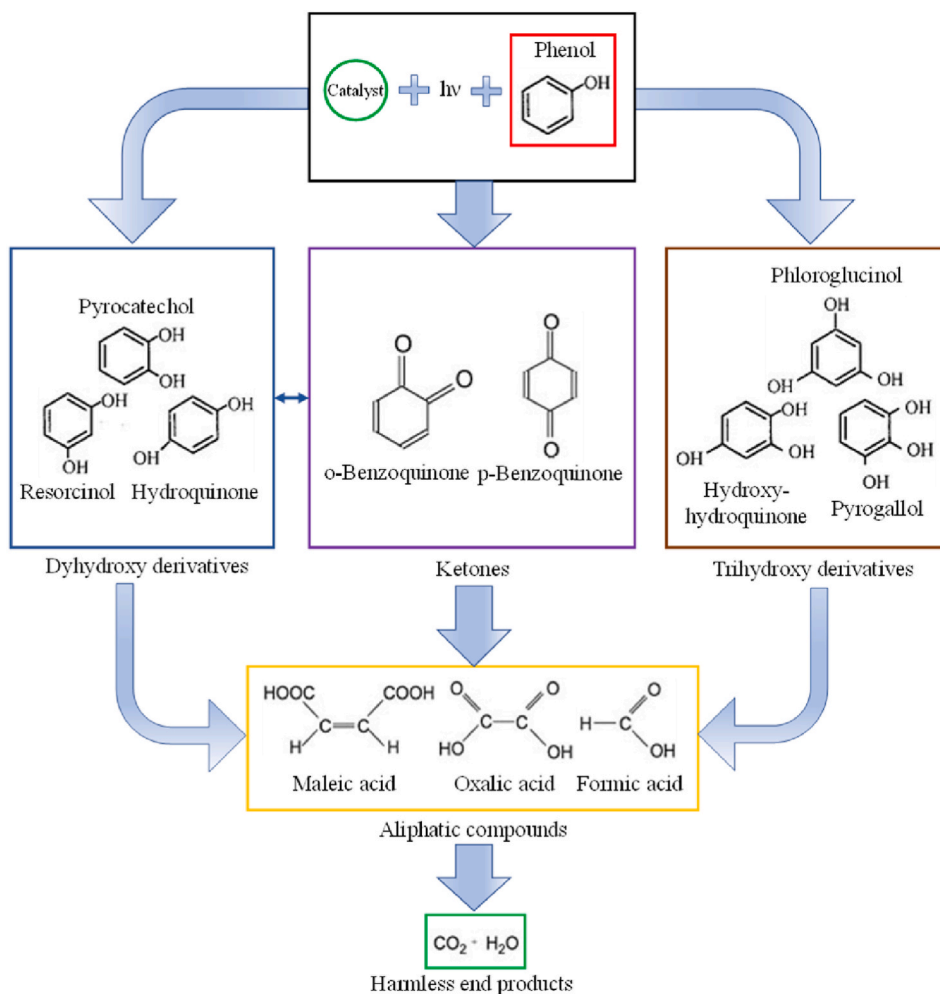


Fig. 7. Possible intermediates of phenol formed during its photocatalytic oxidation [88].

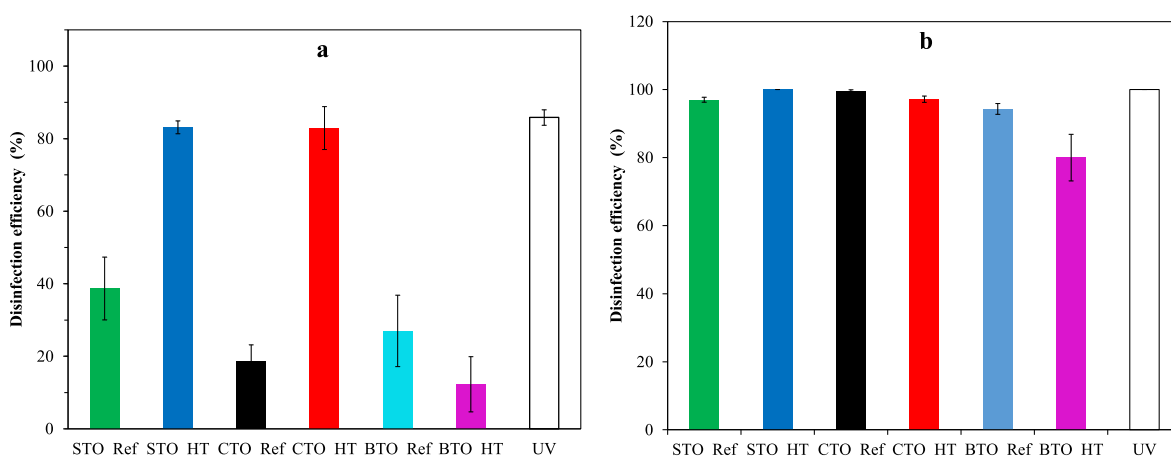


Fig. 8. Photocatalytic inactivation of *E. coli* (a) and *B. licheniformis* (b) bacteria with alkaline earth metal titanates after 120 min of UV-A light irradiation.

hydroxyl radicals can be the reason for their low photocatalytic disinfection inefficiency. For STO_HT and CTO_HT, photocatalytic disinfection efficiency did not decrease; however, it did not increase either. This result can also be associated with their hydroxyl radical generation. These catalysts initially generated ~2.5–4 times more hydroxyl radicals than the other samples. It is plausible that catalysts generating more hydroxyl radicals are more toxic to microorganisms since they do not have enzymatic capacities to neutralize them [30]. The resultant of the

screening effect and generated hydroxyl radicals led to the measured photocatalytic efficiency.

It is also worth highlighting that hydroxyl radical formation settles to a largely constant and similar value for all samples over time. As implied in the previous section, initially, only coumarin is present in the system, so the catalysts can react only with it without competition. Over time, however, intermediates of coumarin form (7-HC in this case), leading to their simultaneous competitive degradation. That is why 7-HC

formation becomes largely constant (Fig. 6) as the generation and degradation steps balance each other out over time.

The disinfection efficiency was also investigated using Gram-positive *Bacillus licheniformis*. Overall, the catalysts possessed higher photocatalytic activity for *B. licheniformis* than for *E. coli*. After only 1 h of UV-A irradiation, 100 % disinfection efficiency was observed for blank UV light, STO_HT, and CTO_HT (Fig. S3). This is the same trend we observed for *E. coli*. In comparison, inactivating *E. coli* bacteria was 20 % less efficient in twice the time. Considering the same periods (i.e., 2 h), all catalysts achieved nearly 100 % bacterial inactivation for *B. licheniformis* (Fig. 8b). These results are in good agreement with the literature as it has been reported that due to the different structure and composition of Gram-positive bacterial cell walls, they are more susceptible to photocatalytic treatment than Gram-negative bacteria [34,90,91]. However, it is important to highlight once again that these apparent high disinfection efficiencies predominantly originate from UV light, and the catalysts either do not change or outright reduce them, as discussed in the first paragraph of this section. For reference, the photocatalytic bacterial inactivation curves (Figs. S4 and S5) and measurements with commercial reference P25 TiO₂ are included in the supplementary material. Last, it is worth mentioning that under visible light no photocatalytic disinfection efficiency can be expected as the band gaps of the catalysts are too wide, preventing their activation and subsequent free radical generation.

In summary, the alkaline earth metal perovskites investigated do not show disinfection properties in the absence of light, while their ability to inactivate bacteria is also fairly limited in the presence of UV light. It is worth reiterating that our main goal with these investigations was to evaluate the disinfection effect of unmodified alkaline earth metal titanates, not to enhance it via various modifications. These perovskite materials are becoming increasingly common due to their different applications [1,61,92–95]. Based on our results (i.e., their efficiency either decreases or remains unchanged under UV light), these perovskites are unlikely to cause harm to microorganisms in surface or groundwater bodies without undergoing structural or other changes. This is particularly the case in the absence of light (e.g., in groundwater), while their disinfection effect is rather poor in the presence of light.

3.2.4. Stability and reusability

The stability of the hydrothermally synthesized catalysts was evaluated by comparing their XRD patterns and SEM micrographs before and after phenol degradation (Fig. S6). No new diffractions were observed, and the morphology did not change either during the photocatalytic evaluation, showing the high stability of the samples. Their reusability was also evaluated via phenol degradation over three cycles (Fig. S7). Exceptional and reasonably high reusability was observed for CTO_HT and BTO_HT, respectively. However, the efficiency of STO_HT decreased significantly (from ~43 % conversion to ~21 % conversion), which can partly be attributed to the unavoidable losses during catalyst recovery. Since the efficiency of CTO_HT and BTO_HT for phenol degradation is rather small, the photoactivity loss from catalyst recovery did not impact their efficiency as significantly.

4. Conclusions

The alkaline earth metal titanates prepared via a hydrothermal method and the commercial references had primary crystallite sizes between 22.2 and 39.2 nm and specific surface areas between 2.1 and 34.0 m² g⁻¹. Hydrothermally synthesized samples contained 4.9–6 % carbonates. The photocatalytic phenol degradation activity of our alkaline earth metal titanates always surpassed that of commercial references. Our strontium titanate performed significantly better than calcium and barium titanates ($r_0 = 41.60$ compared to 4.28 and 10.03 × 10⁻¹⁰ M s⁻¹, respectively). The high photoactivity was attributed to i) the presence of SrCO₃ co-catalyst enhancing charge separation and generating more •OH radicals, ii) the highest specific surface area, and

iii) the favorable valence band position enabling the generation of •OH radicals. The systematic (photocatalytic) disinfection efficiency of alkaline earth metal titanates was investigated for the first time. In the absence of catalysts, UV-A light inactivated ~80 % *E. coli* and 100 % *B. licheniformis* bacteria over 2 and 1 h, respectively. Only the disinfectant effects of CTO_HT and STO_HT were comparable to that of UV-A light, while the other catalysts decreased it by ~30–100 %. These results were attributed to the resultant of the screening effect and the number of generated hydroxyl radicals. The hydrothermally synthesized catalysts proved to be reusable and stable in most cases, except for STO_HT, whose efficiency was halved over three cycles. This study contributes to understanding the potential risks of utilizing alkaline earth metal titanate perovskites across various industries, and thus, to environmental sustainability.

CRedit authorship contribution statement

Tamás Gyulavári: Writing – review & editing, Writing – original draft, Visualization, Supervision, Investigation, Funding acquisition, Conceptualization. **Mahsa Abedi:** Investigation. **Sarolta Tóth:** Investigation. **Áron Ágoston:** Investigation. **Gábor Veréb:** Writing – review & editing, Methodology. **Attila Bodor:** Writing – review & editing, Validation, Methodology, Investigation. **Ákos Kukovecz:** Resources. **Zoltán Kónya:** Resources. **Katalin Perei:** Supervision, Resources. **Zsolt Pap:** Visualization, Conceptualization.

Declaration of competing interest

The authors declare that they have no known competing financial interests or personal relationships that could have appeared to influence the work reported in this paper.

Acknowledgements

This study was financed by the Bolyai János scholarship (BO/00447/23) provided by the Hungarian Academy of Sciences. The authors acknowledge the 2021-1.2.6-TÉT-IPARI-MA-2022-00009 project. Áron Ágoston acknowledges the Doctoral Student Scholarship Program of the Co-operative Doctoral Program (EKÖP-KDP-24-SZTE-6) of the Ministry of Innovation and Technology financed from the National Research, Development and Innovation Fund. Project no. TKP2021-NVA-19 has been implemented with the support provided by the Ministry of Innovation and Technology of Hungary from the National Research, Development and Innovation Fund, financed under the TKP2021-NVA funding scheme.

Appendix A. Supplementary data

Supplementary data to this article can be found online at <https://doi.org/10.1016/j.ceramint.2025.07.286>.

References

- [1] R.R. Solís, J. Bedia, J.J. Rodríguez, C. Belver, A review on alkaline earth metal titanates for applications in photocatalytic water purification, *Chem. Eng. J.* 409 (2021) 128110.
- [2] P. Kanhere, Z. Chen, A review on visible light active perovskite-based photocatalysts, *Molecules* 19 (2014) 19995–20022.
- [3] M. Abedi, Á. Szamosvölgyi, A. Sági, Á. Kukovecz, Z. Kónya, T. Gyulavári, Z. Pap, Influence of rapid heat treatment on the photocatalytic activity and stability of strontium titanates against a broad range of pollutants, *Catalysts* 13 (2023) 219.
- [4] M. Abedi, Z.R. Toth, M. Todea, A. Agoston, A. Kukovecz, Z. Konya, Z. Pap, T. Gyulavári, Influence of rapid heat treatment on the photocatalytic activity and stability of calcium titanates against a broad range of pollutants, *Heliyon* 10 (2024) e34938.
- [5] A. Bhava, U.S. Shenoy, D.K. Bhat, Silver doped barium titanate nanoparticles for enhanced visible light photocatalytic degradation of dyes, *Environ. Pollut.* 344 (2024) 123430.
- [6] B. Moss, Q. Wang, K.T. Butler, R. Grau-Crespo, S. Selim, A. Regoutz, T. Hisatomi, R. Godin, D.J. Payne, A. Kafizas, K. Domen, L. Steier, J.R. Durrant, Linking in situ

- charge accumulation to electronic structure in doped SrTiO₃ reveals design principles for hydrogen-evolving photocatalysts, *Nat. Mater.* 20 (2021) 511–517.
- [7] T. Gyulavári, D. Dusnoki, V. Márta, M. Yadav, M. Abedi, A. Sági, A. Kukovecz, Z. Kónya, Z. Pap, Dependence of photocatalytic activity on the morphology of strontium titanates, *Catalysts* 12 (2022) 523.
- [8] B. Kiss, T.D. Manning, D. Hesp, C. Didier, A. Taylor, D.M. Pickup, A.V. Chadwick, H.E. Allison, V.R. Dhanak, J.B. Claridge, J.R. Darwent, M.J. Rosseinsky, Nanostructured rhodium doped SrTiO₃–Visible light activated photocatalyst for water decontamination, *Appl. Catal. B Environ.* 206 (2017) 547–555.
- [9] H. Zhang, H. Yao, W. Han, Q. Guo, S. Xue, J. Wang, Y. Zhang, Z. Zhang, Transformed construction from type-II WO₃/BaTiO₃ heterojunction to Z-scheme WO₃/Ba_{0.5}Sr_{0.5}TiO₃ and WO₃/SrTiO₃ photocatalytic systems: enhanced photocatalytic activity and mechanism insight, *Ceram. Int.* 50 (2024) 30199–30214.
- [10] P.I. Uma, U.S. Shenoy, D.K. Bhat, Electronic structure engineering of BaTiO₃ cuboctahedrons by doping copper to enhance the photocatalytic activity for environmental remediation, *J. Alloys Compd.* 948 (2023) 169600.
- [11] D.K. Bhat, P.I. Uma, U.S. Shenoy, Exceptional light harvesting in copper doped CaTiO₃ nanocuboids with surface nanosteps for the photo remediation of toxic Cr (VI) ions and dyes, *J. Alloys Compd. Commun.* 4 (2024) 100030.
- [12] D.K. Bhat, U. Pi, U.S. Shenoy, Insights into the dopant engineering in copper-doped SrTiO₃ nanocubes, *J. Hazard. Mater. Adv.* 12 (2023) 100380.
- [13] H. Ren, P. Koshy, W.-F. Chen, S. Qi, C.C. Sorrell, Photocatalytic materials and technologies for air purification, *J. Hazard. Mater.* 325 (2017) 340–366.
- [14] R. Tao, X. Li, X. Li, C. Shao, Y. Liu, TiO₂/SrTiO₃/g-C₃N₄ ternary heterojunction nanofibers: gradient energy band, cascade charge transfer, enhanced photocatalytic hydrogen evolution, and nitrogen fixation, *Nanoscale* 12 (2020) 8320–8329.
- [15] L. Panda, A. Pradhan, E. Subudhi, B. Nanda, Facile fabrication of plasmonic Ag modified CaTiO₃: for boosting photocatalytic reduction of Cr⁶⁺ and antimicrobial study, *Inorg. Chem. Commun.* 150 (2023) 110486.
- [16] M. Yadav, T. Gyulavári, J. Kiss, K.B. Ábrahám, A. Efreanova, Á. Szamosvölgyi, Z. Pap, A. Sági, A. Kukovecz, Z. Kónya, Noble metal nanoparticles and nanodiamond modified strontium titanate photocatalysts for room temperature CO production from direct hydrogenation of CO₂, *J. CO₂ Util.* 78 (2023) 102621.
- [17] U.S. Shenoy, B. Amin, D.K. Bhat, Exploring the impact of modulation of electronic structure via doping in the realm of environmental applications, *Nano Trends* 9 (2025) 100075.
- [18] P.I. Uma, U.S. Shenoy, D.K. Bhat, Doped BaTiO₃ cuboctahedral nanoparticles: role of copper in photocatalytic degradation of dyes, *Appl. Surf. Sci. Adv.* 15 (2023) 100408.
- [19] U.S. Shenoy, P.I. Uma, D.K. Bhat, Copper doping induced band structure and morphology transformation in CaTiO₃ for textile dye photodegradation applications, *J. Alloys Compd.* 1004 (2024) 175779.
- [20] N. Sharma, K. Hernadi, The emerging career of strontium titanates in photocatalytic applications: a review, *Catalysts* 12 (2022) 1619.
- [21] A.L. Linsebigler, G. Lu, J.T. Yates, Photocatalysis on TiO₂ surfaces: principles, mechanisms, and selected results, *Chem. Rev.* 95 (2002) 735–758.
- [22] U.P. I, U.S. Shenoy, D.K. Bhat, Nanocubic copper-doped SrTiO₃ for photoreduction of Cr(VI) and photodegradation of methyl violet, *Appl. Nano. Mater.* 6 (2023) 16798–16804.
- [23] D.K. Bhat, H. Bantawal, U.P. I, U.S. Shenoy, Enhanced photoresponse and efficient charge transfer in porous graphene-BaTiO₃ nanocomposite for high performance photocatalysis, *Diam. Relat. Mater.* 139 (2023) 110312.
- [24] D.K. Bhat, H. Bantawal, P.I. Uma, S.P. Kumar, U.S. Shenoy, Designing sustainable porous graphene-CaTiO₃ nanocomposite for environmental remediation, *Sust. Chem. Environ.* 5 (2024) 100071.
- [25] S. Maiti, I. Fournier, S.K. Brar, M. Cledon, R.Y. Surampalli, Nanomaterials in surface water and sediments: fate and analytical challenges, *J. Hazard. Toxic Radioact. Waste* 20 (2016).
- [26] H. Chen, Metal based nanoparticles in agricultural system: behavior, transport, and interaction with plants, *Chem. Speciat. Bioavailab.* 30 (2018) 123–134.
- [27] K. Solyomos, I. Babcsányi, B. Ariya, T. Gyulavári, Á. Ágoston, Á. Szamosvölgyi, Á. Kukovecz, Z. Kónya, A. Farsang, Z. Pap, Photocatalytic and surface properties of titanium dioxide nanoparticles in soil solutions, *Environ. Sci. Nano* 11 (2024) 1204–1216.
- [28] Q. Abbas, B. Yousaf, Amina, M.U. Ali, M.A.M. Munir, A. El-Naggar, J. Rinklebe, M. Naushad, Transformation pathways and fate of engineered nanoparticles (ENPs) in distinct interactive environmental compartments: a review, *Environ. Int.* 138 (2020) 105646.
- [29] K. Solyomos, E. Kanász, Á. Ágoston, T. Gyulavári, B. Pálffy, Á. Szamosvölgyi, Á. Kukovecz, Z. Kónya, Z. Pap, Impact of different soil solutions on the stability and photocatalytic activity of commercial zinc oxide nanoparticles, *Environ. Sci. Nano* (2025).
- [30] J.A. Imlay, Cellular defenses against superoxide and hydrogen peroxide, *Annu. Rev. Biochem.* 77 (2008) 755–776.
- [31] A. Paleologou, H. Marakas, N.P. Xekoukoulotakis, A. Moya, Y. Vergara, N. Kalogerakis, P. Gikas, D. Mantzavinos, Disinfection of water and wastewater by TiO₂ photocatalysis, sonolysis and UV-C irradiation, *Catal. Today* 129 (2007) 136–142.
- [32] P.V. Laxma Reddy, B. Kavitha, P.A. Kumar Reddy, K.H. Kim, TiO₂-based photocatalytic disinfection of microbes in aqueous media: a review, *Environ. Res.* 154 (2017) 296–303.
- [33] S. Pigeot-Remy, F. Simonet, D. Atlan, J.C. Lazzaroni, C. Guillard, Bactericidal efficiency and mode of action: a comparative study of photochemistry and photocatalysis, *Water Res.* 46 (2012) 3208–3218.
- [34] J.A. Rengifo-Herrera, C. Pulgarin, Why five decades of massive research on heterogeneous photocatalysis, especially on TiO₂, has not yet driven to water disinfection and detoxification applications? Critical review of drawbacks and challenges, *Chem. Eng. J.* 477 (2023) 146875.
- [35] H.A. Foster, I.B. Ditta, S. Varghese, A. Steele, Photocatalytic disinfection using titanium dioxide: spectrum and mechanism of antimicrobial activity, *Appl. Microbiol. Biotechnol.* 90 (2011) 1847–1868.
- [36] E.A. Elgohary, Y.M.A. Mohamed, H.A. El Nazer, O. Baaloudj, M.S.S. Alyami, A. El Jery, A.A. Assadi, A. Amrane, A review of the use of semiconductors as catalysts in the photocatalytic inactivation of microorganisms, *Catalysts* 11 (2021) 1498.
- [37] E. Marin, F. Boschetto, T.P.M. Sunthar, M. Zanocco, E. Ohgitani, W. Zhu, G. Pezzotti, Antibacterial effects of barium titanate reinforced polyvinyl-siloxane scaffolds, *International J. Polym. Mater. Polym. Biomater.* 70 (2020) 425–436.
- [38] D. Xia, Z. Tang, Y. Wang, R. Yin, H. He, X. Xie, J. Sun, C. He, P.K. Wong, G. Zhang, Piezo-catalytic persulfate activation system for water advanced disinfection: process efficiency and inactivation mechanisms, *Chem. Eng. J.* 400 (2020) 125894.
- [39] K.A. Qurbani, O. Amiri, G.M. Othman, A.A. Fatah, N.J. Yunis, M. Joshaghani, S. S. Ahmed, N.A. Abdulrahman, Enhanced antibacterial efficacy through piezo-memorial effect of CaTiO₃/TiO₂ Nano-Composite, *Inorg. Chem. Commun.* 165 (2024) 112470.
- [40] A. Benke, E. Mehner, M. Rosenkranz, E. Dmitrieva, T. Leisegang, H. Stöcker, W. Pompe, D.C. Meyer, Pyroelectrically driven •OH generation by barium titanate and Palladium nanoparticles, *J. Phys. Chem. C* 119 (2015) 18278–18286.
- [41] M. Sharma, G. Singh, R. Vaish, Dye degradation and bacterial disinfection using multicalcic BaZr_{0.02}Ti_{0.98}O₃ ceramics, *J. Am. Ceram. Soc.* 103 (2020) 4774–4784.
- [42] J. Chen, X. Guo, L. Lang, X. Yin, A. Wang, Z. Rui, Multifunctional Z-scheme Cu_xO/Ag/SrTiO₃ heterojunction for photothermocatalytic VOCs degradation and antibiosis, *Appl. Surf. Sci.* 618 (2023) 153275.
- [43] S. Usuki, S. Machida, K.-i. Katsumata, M. Ogawa, S.S. Latthe, S. Liu, K. Yamatoya, K. Nakata, Mechanism of selective Qβ Bacteriophage inactivation under the presence of E. Coli using ground Rh-doped SrTiO₃ photocatalyst, *Catalysts* 14 (2024) 94.
- [44] Y. Yamaguchi, S. Usuki, Y. Kanai, K. Yamatoya, N. Suzuki, K.I. Katsumata, C. Terashima, T. Suzuki, A. Fujishima, H. Sakai, A. Kudo, K. Nakata, Selective inactivation of Bacteriophage in the presence of bacteria by use of ground Rh-doped SrTiO₃ photocatalyst and visible light, *ACS Appl. Mater. Interfaces* 9 (2017) 31393–31400.
- [45] H.S. Bae, R.P. Patil, J.H. Hwang, M.A. Mahadik, M.S. Song, W.-S. Chae, V. Manikandan, J.S. Jang, Visible-light-responsive hydrogen-reduced Co_x loaded Rh/Sb:SrTiO₃ nanocubic photocatalyst for degradation of organic pollutants and inactivation of bacteria, *J. Environ. Chem. Eng.* 11 (2023) 109837.
- [46] S. Kumar, M. Sharma, A. Kumar, S. Powar, R. Vaish, Rapid bacterial disinfection using low frequency piezocatalysis effect, *J. Ind. Eng. Chem.* 77 (2019) 355–364.
- [47] D. Jiang, X. Sun, X. Wu, L. Shi, F. Du, Hydrothermal synthesis of single-crystal Cr-doped SrTiO₃ for efficient visible-light responsive photocatalytic hydrogen evolution, *Mater. Res. Express* 7 (2020) 015047.
- [48] D. Flak, A. Braun, B.S. Mun, J.B. Park, M. Parlinska-Wojtan, T. Graule, M. Rekas, Spectroscopic assessment of the role of hydrogen in surface defects, in the electronic structure and transport properties of TiO₂, ZnO and SnO₂ nanoparticles, *Phys. Chem. Chem. Phys.* 15 (2013) 1417–1430.
- [49] A. Bodor, N. Bounedjoum, G. Feigl, A. Duzs, K. Laczi, A. Szilagy, G. Rakhely, K. Perei, Exploitation of extracellular organic matter from *Micrococcus luteus* to enhance ex situ bioremediation of soils polluted with used lubricants, *J. Hazard. Mater.* 417 (2021) 125996.
- [50] Y.S. Huo, H. Yang, T. Xian, J.L. Jiang, Z.Q. Wei, R.S. Li, W.J. Feng, A polyacrylamide gel route to different-sized CaTiO₃ nanoparticles and their photocatalytic activity for dye degradation, *J. Sol. Gel Sci. Technol.* 71 (2014) 254–259.
- [51] C. Han, J. Liu, W. Yang, Q. Wu, H. Yang, X. Xue, Photocatalytic activity of CaTiO₃ synthesized by solid state, sol-gel and hydrothermal methods, *J. Sol. Gel Sci. Technol.* 81 (2016) 806–813.
- [52] B. Boga, V.-M. Cristea, I. Székely, F. Lorenz, T. Gyulavári, L.C. Pop, L. Baia, Z. Pap, N. Steinfeldt, J. Strunk, Experimental data-driven and phenomenological modeling approaches targeting the enhancement of CaTiO₃ photocatalytic efficiency, *Sustain. Chem. Pharm.* 33 (2023) 101045.
- [53] M.-V. Le, N.-Q.-D. Vo, Q.-C. Le, V.A. Tran, T.-Q.-P. Phan, C.-W. Huang, V.-H. Nguyen, Manipulating the structure and characterization of Sr_{1-x}La_xTiO₃ nanocubes toward the photodegradation of 2-Naphthol under artificial solar light, *Catalysts* 11 (2021) 564.
- [54] Z.Z. Lazarević, M. Vijatović, Z. Dohčević-Mitrović, N.Z. Romčević, M.J. Romčević, N. Paunović, B.D. Stojanović, The characterization of the barium titanate ceramic powders prepared by the Pechini type reaction route and mechanically assisted synthesis, *J. Eur. Ceram. Soc.* 30 (2010) 623–628.
- [55] C. Bogjcević, G. Thörner, F. Karolák, P. Haghi-Ashtiani, J.M. Kiat, Morphogenesis mechanisms in the solvothermal synthesis of BaTiO₃ from titanate nanorods and nanotubes, *Nanoscale* 7 (2015) 3594–3603.

- [56] M.C. Reis, M.F.B. Sousa, F. Alobaid, C.A. Bertran, Y. Wang, A two-fluid model for calcium carbonate precipitation in highly supersaturated solutions, *Adv. Powder Technol.* 29 (2018) 1571–1581.
- [57] Z. Asgari-Fard, M. Sabet, M. Salavati-Niasari, Synthesis and characterization of strontium carbonate nanostructures via simple hydrothermal method, *High Temp. Mater. Process.* 35 (2016) 215–220.
- [58] L.F. da Silva, L.J.Q. Maia, M.L.B. Bernardi, J.A. Andrés, V.R. Mastelaro, An improved method for preparation of SrTiO₃ nanoparticles, *Mater. Chem. Phys.* 125 (2011) 168–173.
- [59] A. Sivakumar, S. Kalaiarasi, S.S.J. Dhas, A.I. Almansour, R.S. Kumar, N. Arumugam, S.A.M.B. Dhas, Assessment of shock wave resistance on brookite TiO₂, *J. Mater. Sci. Mater. Electron.* 32 (2021) 15134–15142.
- [60] N. Hashemi, H.Q. Alijani, F. Mousazadeh, S. Rahi, S. Darijani, F. Sharifi, H. Khalili, S. Irvani, F. Borhani, N. Zafarnia, M. Khatami, Leishmanicidal activities of biosynthesized BaCO₃ (witherite) nanoparticles and their biocompatibility with macrophages, *Bioproc. Biosyst. Eng.* 44 (2021) 1957–1964.
- [61] B.L. Phoon, C.W. Lai, J.C. Juan, P.L. Show, W.H. Chen, A review of synthesis and morphology of SrTiO₃ for energy and other applications, *Int. J. Energy Res.* 43 (2019) 5151–5174.
- [62] S.-T. Huang, W.W. Lee, J.-L. Chang, W.-S. Huang, S.-Y. Chou, C.-C. Chen, Hydrothermal synthesis of SrTiO₃ nanocubes: characterization, photocatalytic activities, and degradation pathway, *J. Taiwan Inst. Chem. Eng.* 45 (2014) 1927–1936.
- [63] B. Boga, N. Steinfeldt, N.G. Moustakas, T. Peppel, H. Lund, J. Rabeah, Z. Pap, V.-M. Cristea, J. Strunk, Role of SrCO₃ on photocatalytic performance of SrTiO₃-SrCO₃ composites, *Catalysts* 12 (2022) 978.
- [64] J.S. Jang, P.H. Borse, J.S. Lee, K.T. Lim, O.S. Jung, E.D. Jeong, J.S. Bae, H.G. Kim, Photocatalytic hydrogen production in water-methanol mixture over Iron-doped CaTiO₃, *Bull. Kor. Chem. Soc.* 32 (2011) 95–99.
- [65] B.L. Phoon, C.W. Lai, J.C. Juan, P.-L. Show, G.-T. Pan, Recent developments of strontium titanate for photocatalytic water splitting application, *Int. J. Hydrogen Energy* 44 (2019) 14316–14340.
- [66] A.M. Youssef, H.K. Farag, A. El-Kheshen, F.F. Hammad, Synthesis of nano-structured strontium titanate by sol-gel and solid state Routes, *Silicon* 10 (2017) 1225–1230.
- [67] M.G. Elmahgary, A.M. Mahran, M. Ganoub, S.O. Abdellatif, Optical investigation and computational modelling of BaTiO₃ for optoelectronic devices applications, *Sci. Rep.* 13 (2023) 4761.
- [68] K. Suzuki, K. Kijima, Optical band gap of barium titanate nanoparticles prepared by RF-plasma chemical Vapor deposition, *Jpn. J. Appl. Phys.* 44 (2005) 2081.
- [69] P. Chen, X. Li, Z. Ren, J. Wu, Y. Li, W. Liu, P. Li, Y. Fu, J. Ma, Enhancing photocatalysis of Ag nanoparticles decorated BaTiO₃ nanofibers through Plasmon-induced resonance energy transfer turned by piezoelectric field, *Catalysts* 12 (2022) 987.
- [70] T. Xian, H. Yang, L. Di, J. Ma, H. Zhang, J. Dai, Photocatalytic reduction synthesis of SrTiO₃-graphene nanocomposites and their enhanced photocatalytic activity, *Nanoscale Res. Lett.* 9 (2014) 327.
- [71] J.H. Roque-Ruiz, J. Meraz-Angel, R. Farias, M. Melendez-Lira, S.Y. Reyes-Lopez, Sol-Gel synthesis of strontium titanate nanofibers by Electrospinning, *J. Ceram. Sci. Technol.* 10 (2019) 29–37.
- [72] D. Kothandan, R. Jeevan Kumar, K. Chandra Babu Naidu, Barium titanate microspheres by low temperature hydrothermal method: studies on structural, morphological, and optical properties, *J. Asian Ceram. Soc.* 6 (2018) 1–6.
- [73] S.A.U. Portia, R. Srinivasan, E. Elaiyappillai, P.M. Johnson, K. Ramamoorthy, Facile synthesis of Eu-doped CaTiO₃ and their enhanced supercapacitive performance, *Ionics* 26 (2020) 3543–3554.
- [74] A.B.D. Nandiyanto, R. Oktiani, R. Ragadhita, How to read and interpret FTIR spectroscopy of organic material, *Indonesian J. Sci. Technol.* 4 (2019) 97.
- [75] J. Orlikowski, B. Tryba, J. Ziebro, A.W. Morawski, J. Przepiórski, A new method for preparation of rutile phase titania photoactive under visible light, *Catal. Commun.* 24 (2012) 5–10.
- [76] X. Ye, C. Zheng, L. Ma, X. Huang, Microemulsion-assisted hydrothermal preparation and infrared radiation property of TiO₂ nanomaterials with tunable morphologies and crystal form, *Mater. Sci. Semicond. Process.* 31 (2015) 295–301.
- [77] Y. Fo, Y. Ma, H. Dong, X. Zhou, Tuning the electronic structure of BaTiO₃ for an enhanced photocatalytic performance using cation–anion codoping: a first-principles study, *New J. Chem.* 45 (2021) 8228–8239.
- [78] X.T. Mai, D.N. Bui, V.K. Pham, T.H.L. Nguyen, T.T.L. Nguyen, H.D. Chau, T.K. N. Tran, Effect of CuO loading on the photocatalytic activity of SrTiO₃ for hydrogen evolution, *Inorganics* 10 (2022) 130.
- [79] X. Gao, M. Song, D. Sun, R. Guan, H. Zhai, Z. Zhao, Q. Zhang, X. Li, A facile in situ hydrothermal Etching method to CaTiO₃/TiO₂ Heterostructure for efficient photocatalytic N₂ reduction, *Catal. Lett.* 152 (2021) 1990–1998.
- [80] J.-i. Fujisawa, T. Eda, M. Hanaya, Comparative study of conduction-band and valence-band edges of TiO₂, SrTiO₃, and BaTiO₃ by ionization potential measurements, *Chem. Phys. Lett.* 685 (2017) 23–26.
- [81] G.X. Castillo-Cabrera, C.I. Pliego-Cerdan, E. Mendez, P.J. Espinoza-Montero, Step-by-step guide for electrochemical generation of highly oxidizing reactive species on BDD for beginners, *Front. Chem.* 11 (2023) 1298630.
- [82] F. Parrino, S. Livraghi, E. Giamello, R. Cecatto, L. Palmisano, Role of hydroxyl, superoxide, and nitrate radicals on the fate of Bromide ions in photocatalytic TiO₂ suspensions, *ACS Catal.* 10 (2020) 7922–7931.
- [83] K. Lv, X. Guo, X. Wu, Q. Li, W. Ho, M. Li, H. Ye, D. Du, Photocatalytic selective oxidation of phenol to produce dihydroxybenzenes in a TiO₂/UV system: hydroxyl radical versus hole, *Appl. Catal. B Environ.* 199 (2016) 405–411.
- [84] G. Veréb, L. Manczinger, G. Bozsó, A. Sienkiewicz, L. Forró, K. Mogyorósi, K. Hernádi, A. Dombi, Comparison of the photocatalytic efficiencies of bare and doped rutile and anatase TiO₂ photocatalysts under visible light for phenol degradation and E. coli inactivation, *Appl. Catal. B Environ.* 129 (2013) 566–574.
- [85] M. Náfrádi, L. Farkas, T. Alapi, K. Hernádi, K. Kovács, L. Wojnárovits, E. Takács, Application of coumarin and coumarin-3-carboxylic acid for the determination of hydroxyl radicals during different advanced oxidation processes, *Radiat. Phys. Chem.* 170 (2020) 108610.
- [86] Y. Xu, M.A.A. Schoonen, The absolute energy positions of conduction and valence bands of selected semiconducting minerals, *Am. Mineral.* 85 (2000) 543–556.
- [87] P. Górska, A. Zaleska, J. Hupka, Photodegradation of phenol by UV/TiO₂ and Vis/N-C-TiO₂ processes: comparative mechanistic and kinetic studies, *Sep. Purif. Technol.* 68 (2009) 90–96.
- [88] T. Gyulavári, G. Vereb, Z. Pap, B. Reti, K. Baan, M. Todea, K. Magyari, I.M. Szilagyi, K. Hernadi, Utilization of Carbon Nanospheres in photocatalyst production: from composites to highly active Hollow structures, *Materials* 12 (2019).
- [89] D. Vione, C. Minero, V. Maurino, M.E. Carloti, T. Picatonotto, E. Pelizzetti, Degradation of phenol and benzoic acid in the presence of a TiO₂-based heterogeneous photocatalyst, *Appl. Catal. B Environ.* 58 (2005) 79–88.
- [90] P.K. Robertson, J.M. Robertson, D.W. Bahnemann, Removal of microorganisms and their chemical metabolites from water using semiconductor photocatalysis, *J. Hazard. Mater.* 211–212 (2012) 161–171.
- [91] H.M. Yadav, J.-S. Kim, S.H. Pawar, Developments in photocatalytic antibacterial activity of nano TiO₂: a review, *Kor. J. Chem. Eng.* 33 (2016) 1989–1998.
- [92] M. Passi, B. Pal, A review on CaTiO₃ photocatalyst: activity enhancement methods and photocatalytic applications, *Powder Technol.* 388 (2021) 274–304.
- [93] J. Gao, D. Xue, W. Liu, C. Zhou, X. Ren, Recent progress on BaTiO₃-based piezoelectric ceramics for Actuator applications, *Actuators* 6 (2017) 24.
- [94] F.E. Bouharras, M. Raihane, B. Ameduri, Recent progress on core-shell structured BaTiO₃@polymer/fluorinated polymers nanocomposites for high energy storage: synthesis, dielectric properties and applications, *Prog. Mater. Sci.* 113 (2020) 100670.
- [95] D. Masekela, N.C. Hintsho-Mbita, S. Sam, T.L. Yusuf, N. Mabuba, Application of BaTiO₃-based catalysts for piezocatalytic, photocatalytic and piezo-photocatalytic degradation of organic pollutants and bacterial disinfection in wastewater: a comprehensive review, *Arab. J. Chem.* 16 (2023) 104473.